ACS NANO

www.acsnano.org

Article

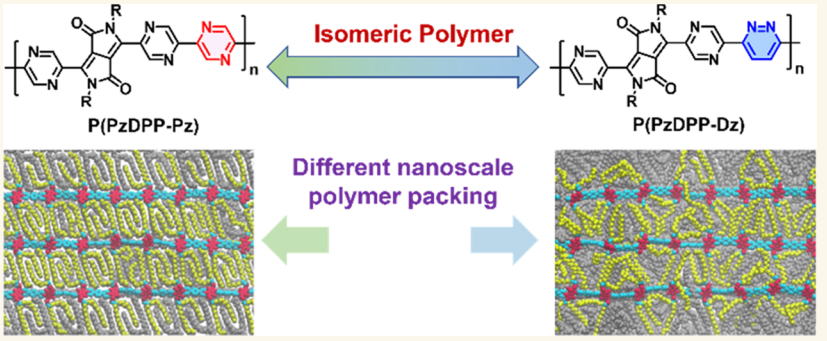
Realizing Ultralow Energetic Disorder and High Thermoelectric Performances via Nanoscale Polymer Packing Control

Jia-Tong Li,[▽] Guangchao Liu,*[,▽] Chunlin Xu,[▽] Juan-Rong Wang, Zhuoqiong Zhang, Yunfei Wang, Zhiqiang Cao, Yin Liang, Xin-Yu Deng, Miao Xiong, Xue-Qing Wang, Kai-Kai Liu, Qing Zhang, Xiaodan Gu, Shu Kong So, Chuan-Ding Dong, Kai Lin Woon, Dong Wang,* Zhi Zhang,* and Ting Lei*

Cite This: *ACS Nano* 2026, 20, 11545–11557

Read Online

ACCESS | Metrics & More | Article Recommendations | Supporting Information



ABSTRACT: Charge transport and thermoelectric (TE) properties of conjugated polymers are largely determined by their solid-state energetic disorders. Previous studies have focused on the energetic disorders or traps that result from dihedral angle rotations of the polymer backbone. However, this fails to explain the largely different charge transport properties in many conjugated polymers. Here, we investigate the charge transport and TE properties of two isomeric polymers with highly rigid backbones and low energetic disorders along the chain. Both polymers have similar ultralow charge transport activation energies (<35 meV), but exhibit vastly different charge transport properties. We found that P(PzDPP-Pz) with a linear backbone exhibited a high n-type TE power factor, over 2 orders of magnitude higher than its isomer P(PzDPP-Dz). By utilizing multiple characterizations and molecular simulations, we, for the first time, rule out the well-known dihedral-angle rotation disorders and unveil that the disorders and traps originate from the nanoscale polymer packing structures. Our work provides insight into the origins of the various types of disorders and traps across multilevel nanoscale structures in polymer semiconductors.

KEYWORDS: *conjugated polymers, nanoscale polymer packing, organic thermoelectrics, charge transport, energetic disorders*

INTRODUCTION

Conjugated polymers are intriguing for next-generation flexible/stretchable electronics, such as displays, logic circuits, renewable energy, sensors, and other healthcare applications, because they have rich optoelectronic properties and outstanding mechanical properties and can be solution-processed at low temperatures.[1−4] Recent theoretical and experimental studies have suggested that energetic disorders in conjugate polymers are one of the major parameters that limit the charge transport in conjugated polymers.[5−7] Polymers with low energetic disorders are essential for achieving high power factors (PFs) in organic thermoelectrics.[7−9] However, developing low-energy disorder polymers is largely limited by the lack of understanding of energy disorder sources. Thus, understanding the origin of different types of energetic disorders is crucial for achieving efficient charge transport and high device performance.

Conjugated polymer films can be viewed as possessing multilevel nanoscale structures, spanning from molecular-scale backbone conformations to long-range supramolecular arrangements.[10] The primary structure refers to the polymer backbone defined by covalent bonds, such as the dihedral angles between repeating units, that determine molecular planarity and π-electron delocalization. The secondary structure arises from interchain interactions, including $\pi-\pi$ stacking and lamellar packing, which govern intermolecular coupling and the formation of polymer aggregates. The tertiary

Received: July 31, 2025
Revised: March 31, 2026
Accepted: March 31, 2026
Published: April 7, 2026



Downloaded from pubs.acs.org/ancac3/article-pdf/20/15/11545/6504759/nn5c13008.pdf by PEKING UNIV user on 23 November 2026

ACS Publications

© 2026 American Chemical Society

https://doi.org/10.1021/acsnano.5c13008
ACS Nano 2026, 20, 11545−11557

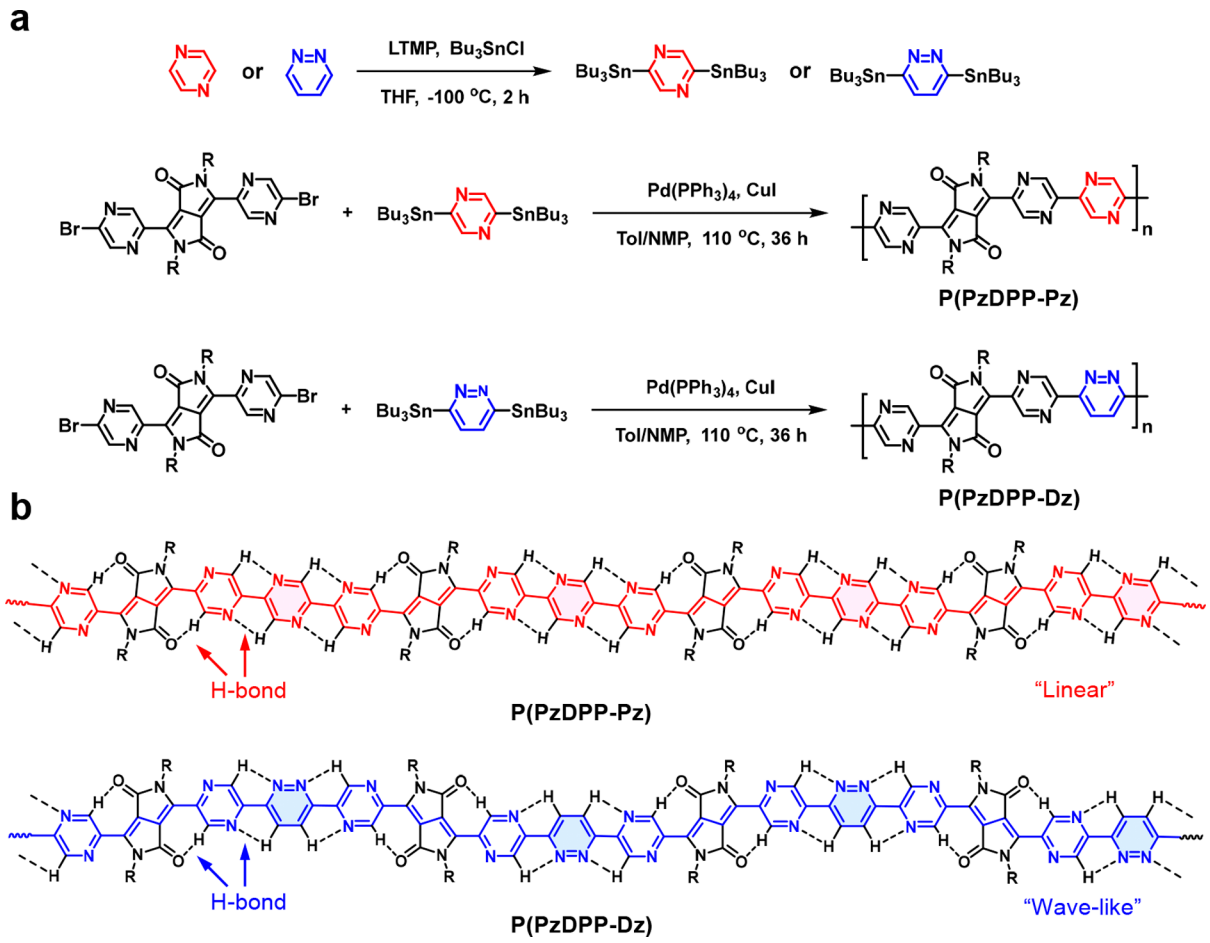


Figure 1. Polymer design, synthesis, and backbone curvature. (a) Synthetic routes and chemical structures of the ditin monomers and the corresponding isomeric polymers, P(PzDPP-Pz) and P(PzDPP-Dz). (b) Schematic illustration of the fully "conformation locked" backbones and the most stable backbone conformations for P(PzDPP-Pz) and P(PzDPP-Dz). *R* = 4-tetradecyloctadecyl.

structure describes the mesoscale phase morphology composed of crystalline and amorphous regions, their orientation, and domain connectivity, which together dictate the macroscopic charge-transport pathways in thin films. The major sources of energetic disorder in conjugated polymers have recently been identified to be the conformational disorders caused by the dihedral angles along polymer chains.[7,8] Recent studies have demonstrated that controlling primary conformational disorder—for instance, by designing rigid and planar backbones with high torsional barriers—can effectively suppress energetic disorder and enhance transport, leading to improved charge carrier mobilities and highly doped electrical conductivities.[6,11−17] For example, a near-amorphous conjugated polymer, indacenodithiophene-*co*-benzothiadiazole (IDTBT), with a planar, torsion-free backbone conformation, exhibited a low degree of energetic disorder, of which the charge transport properties approach intrinsic disorder-free limits.[7] Experiments and molecular dynamics (MD) simulations also prove that the low degree of energetic disorder originates from the remarkable resilience to backbone rotational disorders. Nevertheless, similar rigid IDT-based polymers often display contradictory behaviors, showing largely different energetic disorder or performance despite comparable backbone rigidity.[13] Therefore, these results suggest that the source of these energetic disorders and their correlation with multilevel nanoscale structures and arrangements remains obscure.

To rule out the widely recognized energetic disorders caused by dihedral angles, here, we designed two isomeric polymers with similarly low backbone rotational disorders to explore energetic disorders and their effects on TE performances. Both polymers have identical chemical compositions as well as similar high dihedral angle potentials and frontier orbital energy levels. Because of the merely different positions of nitrogen atoms on the "donor" moiety, polymer P(PzDPP-Pz) has a linear backbone, while the other polymer P(PzDPP-Dz) has a wavy backbone (Figure 1b), which contributes to the different polymer packings. We found that the polymers have different types of energetic disorders and traps in the solid state. P(PzDPP-Pz) exhibits extremely low energy disorder and displays near-ideal charge transport properties and remarkable thermoelectric performances with a high n-type TE PF of 65.6 μW m^{-1} K^{-2}. MD simulations further showed that the linear backbone curvature of P(PzDPP-Pz) resulted in better nanoscale molecular packing, smaller energetic disorders, and fewer traps. In addition to the dihedral angle rotational disorder, we demonstrate that controlling the multilevel nanoscale structures of polymers is also crucial for mitigating energetic disorders in conjugated polymers.

https://doi.org/10.1021/acsnano.5c13008
ACS Nano 2026, 20, 11545−11557

Downloaded from pubs.acs.org/ancac3/article-pdf/20/15/11545/6504759/8/nn5c13008.pdf by PEKING UNIV user on 23 November 2026

Table 1. Summary of the Polymer Properties, Device Performance, and Molecular Packings of the Polymers

polymer	M_n (kDa)	PDI	E_g[a] (eV)	E_{HOMO}[b] (eV)	E_{LUMO}[b] (eV)	σ_{max}[c] (S cm^{-1})	PF_{max}[c] (μW m^{-1} K^{-2})	$d_{lamellar}$[d] (Å)	$d_{\pi-\pi}$[d] (Å)
P(PzDPP-Pz)	39.3	2.95	1.68	−5.78	−3.83	60.5	65.6	29.92	3.34
P(PzDPP-Dz)	42.7	2.78	1.74	−5.74	−3.85	0.15	0.44	29.92	3.51

[a]Calculated from the onset of the absorption spectra of the films. [b]Calculated from the cyclic voltammetry (CV) measurements. [c]Electrical conductivities and thermoelectric performances. [d]Calculated lamellar and $\pi-\pi$ stacking distances from grazing incidence wide-angle X-ray scattering (GIWAXS).

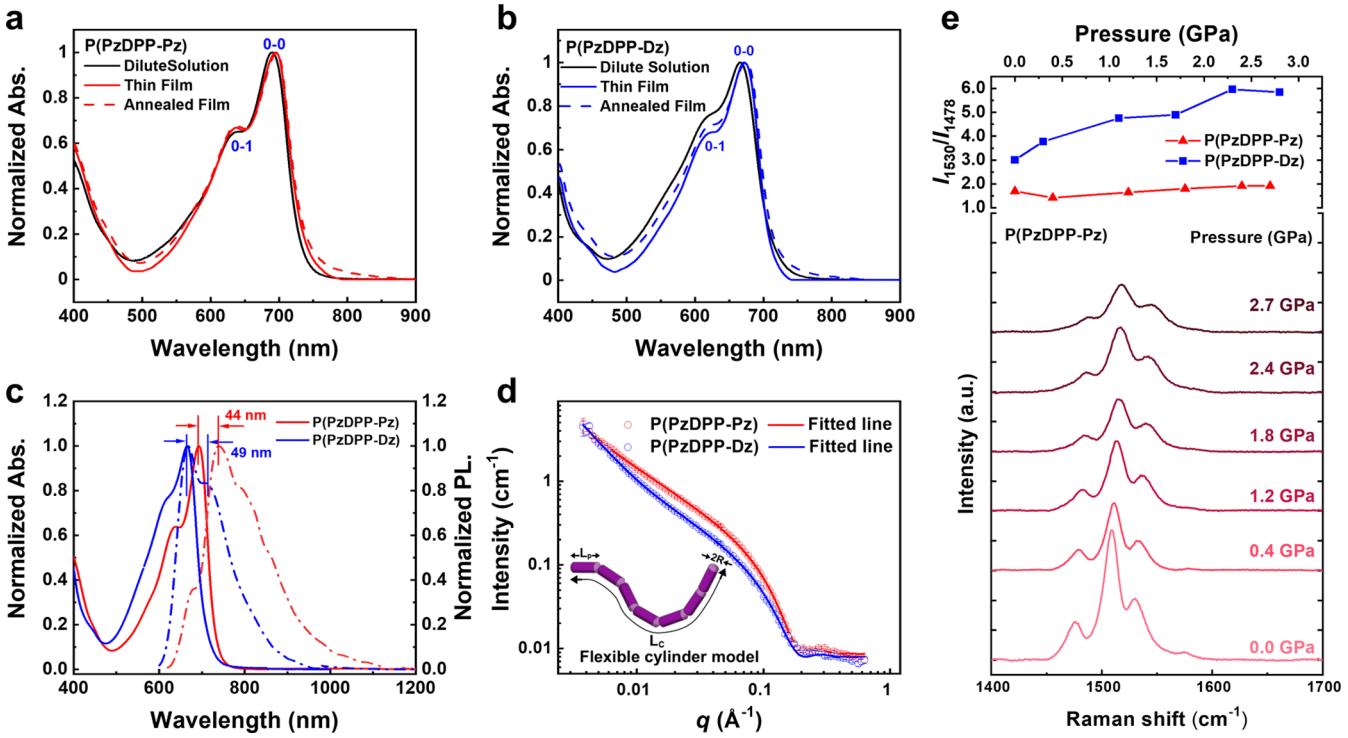


Figure 2. Comparison of the optical properties, aggregation behavior, and interchain interactions. (a, b) Normalized absorption spectra of P(PzDPP-Pz) and P(PzDPP-Dz) in solution, thin film, and annealed film. (c) Normalized absorption (solid lines) and PL (dashed lines) (P(PzDPP-Pz): λ_{ex} = 580 nm, P(PzDPP-Dz): λ_{ex} = 560 nm) spectra of the polymer solutions. (d) Measured small-angle neutron scattering (SANS) data of both polymers in solution at 25 °C. Inset: diagram of the Flexible cylinder model of the polymers in solution obtained from the analysis of the SANS data. Contour length, Kuhn length, and R are used to describe the shape of the polymer aggregates. (e) Pressure dependence of the Raman intensity ratio between the stretching mode of the Pz or Dz ring (1530 cm^{-1}) and the stretching mode of the DPP ring (1478 cm^{-1}) of both polymers (top) and the Raman spectrum of P(PzDPP-Pz) measured using a diamond-anvil cell (bottom). a.u., arbitrary units.

RESULTS AND DISCUSSION

Polymer Design and Synthesis

Previous studies have suggested that good coplanarity of backbone, high and steep dihedral angle potentials, and a single preferential planar backbone conformation are essential for restraining the polymer backbone to maintain a coplanar conformation and enhance tolerance to dopant-induced disorders.[7,8,13,18] Noncovalent interactions and conformational locks are often employed to achieve these features.[19,20] Computational studies have shown that the nitrogen−hydrogen (CH···N) interaction is one of the strongest noncovalent interactions.[21] Inspired by these studies, we designed two new building blocks, pyrazine (Pz) and pyridazine (Dz), for "acceptor−acceptor" type conjugated polymers. Relaxed potential energy scans of the dihedral angles of pyrazine with different building block combinations found that the pyrazine (Pz)-pyrazine (Pz) and pyrazine (Pz)-pyridazine (Dz) combination showed the steepest and the highest dihedral angle potentials among all the segment combinations (Figure S1, Supporting Information). Meanwhile, these backbone combinations have only a predominant conformation at a torsion angle of 0°. Based on these building blocks, two isomeric polymers, P(PzDPP-Pz) and P(PzDPP-Dz), were designed (Figure 1a). PzDPP was employed because of its strong electron-withdrawing properties and good electron mobilities.[22] The two polymers exhibit a planar, conformation-locked, and rigid backbone. Density functional theory (DFT) calculations show that both polymers have small dihedral angles ($\varphi_1-\varphi_4$) in the optimized structures (Figure S2, Supporting Information) due to the O···H and N···H noncovalent interactions. It is worth noting that the two isomeric polymers with only different nitrogen positions show completely distinct backbone curvature based on a single repeating unit (Figure 1b, and see detailed discussions in Section 3 of the Supporting Information).

Generally, thiophene and vinyl derivatives are frequently selected as donor units in D−A conjugated polymers, and electron-withdrawing groups such as cyano and halogen atoms (F, Cl, Br) are usually introduced to modify the donor units to decrease the LUMO levels.[10,23−27] However, other electron-deficient donor units are rarely developed, probably due to the

https://doi.org/10.1021/acsnano.5c13008
ACS Nano 2026, 20, 11545−11557

Downloaded from pubs.acs.org/ancac3/article-pdf/20/15/11545/6504759/nn5c13008.pdf by PEKING UNIV user on 23 November 2026

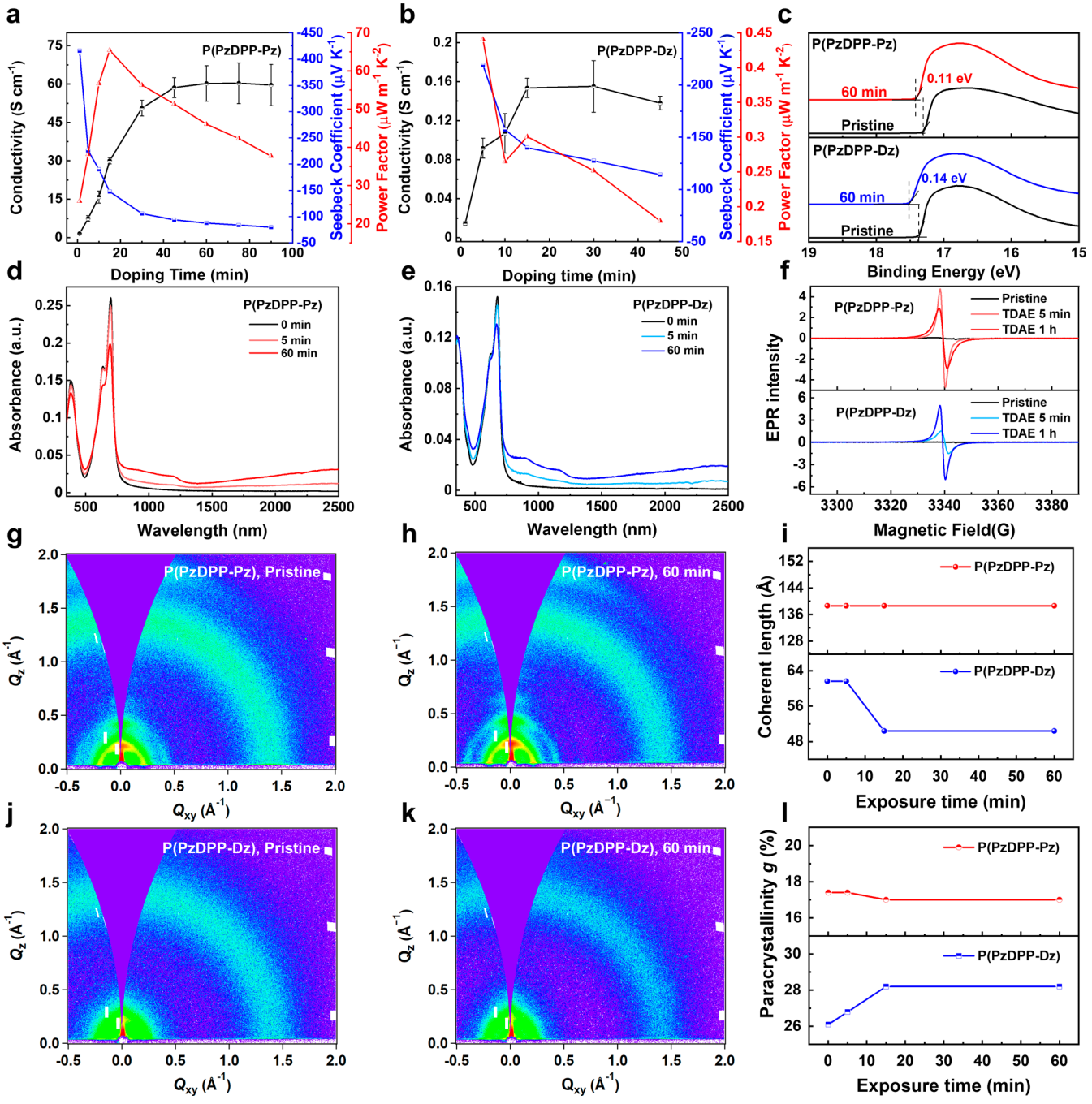


Figure 3. Comparison of n-doped electrical conductivities, Seebeck coefficients, PFs, doping efficiency, and molecular packing behavior. (a, b) Electrical conductivities, Seebeck coefficients, and PFs of P(PzDPP-Pz) and P(PzDPP-Dz) after different exposure times in TDAE vapor (doping time). (c) Ultraviolet photoelectron spectroscopy (UPS) binding energy of the pristine and TDAE-doped films. (d, e) Absorption spectrum changes of the pristine (0 min) and TDAE-doped (5 and 60 min) P(PzDPP-Pz) and P(PzDPP-Dz) films. (f) Electron paramagnetic resonance (EPR) signals of the pristine and TDAE-doped films at different doping times. 2D-GIWAXS patterns of the pristine and TDAE-doped (60 min) (g, h) P(PzDPP-Pz) and (j, k) P(PzDPP-Dz) films. Comparison of (i) the coherent lengths and (l) the paracrystalline disorders of the polymers evaluated at different TDAE exposure times.

difficulty in synthesizing the corresponding tin reagents and borates. Here, the tin reagents of electron-deficient "donor" moieties pyrazine or pyridazine were synthesized ingenuously by using the so-called "in situ trapping technique":[28] pyrazine or pyridazine was lithiated in situ with an excess of LTMP at low temperatures (−100 °C), while tributyltin chloride was used as the electrophile simultaneously, and the tin reagent of pyrazine or pyridazine was obtained in good yield. Two polymers were synthesized via the Pd-catalyzed Stille coupling reaction in the presence of a small amount of CuI as the cocatalyst. We cannot obtain high molecular weight products with the commonly used catalyst composition $Pd_2(dba)_3/P(o\text{-}Tol)_3$. Thus, $Pd(PPh_3)_4$ was screened as a suitable catalyst. Both polymers were purified by Soxhlet extraction, and they also have similar molecular weights (M_w) around 40 kDa, which were evaluated by high-temperature gel permeation chromatography at 150 °C using 1,2,4-trichlorobenzene (TCB) as the eluent (Table 1). Both polymers show excellent

https://doi.org/10.1021/acsnano.5c13008
ACS Nano 2026, 20, 11545−11557

Downloaded from pubs.acs.org/ancac3/article-pdf/20/15/11545/6504759/8/nn5c13008.pdf by PEKING UNIV user on 23 November 2026

thermal stability with decomposition temperatures over 350 °C and no obvious phase transition in the range from room temperature to 300 °C (Figures S4 and S5; Supporting Information).

Polymer Properties and Solution-State Aggregation Behaviors

According to the CV measurement, the estimated LUMO energy levels of P(PzDPP-Pz) and P(PzDPP-Dz) are very similar (−3.83 eV and −3.85 eV) (Table 1 and Figure S6, Supporting Information), since the two polymers have identical chemical structures. In addition, both polymers exhibit similar absorption features in UV−vis absorption spectroscopy (Figure 2a,b). P(PzDPP-Pz) has an absorption peak at 693 nm and a shoulder peak at 640 nm, while P(PzDPP-Dz) has a blue-shifted maximum absorption peak at 665 nm with a shoulder peak at 624 nm in solution. Both polymers show slightly red-shifted absorption spectra when going from solution to film, suggesting that they both adopt planar backbones in solution and the solid state. To gain a deeper understanding of the stiffness and geometric changes of the polymer chains, the spectra were fitted by Franck−Condon progression.[29−38] The spectral changes and Huang−Rhys factor (S) of P(PzDPP-Pz) in solution are smaller, suggesting a stronger aggregation tendency and more rigid and coplanar backbone conformation (see Figure S7 and Table S1 for a detailed discussion, Supporting Information). Temperature-dependent absorption spectra revealed that both polymers showed strong aggregation behaviors even in dilute (1.0×10^{-5} mol L^{-1}) 1-chloronaphthalene (CN) solutions from room temperature to 200 °C, and P(PzDPP-Pz) exhibited stronger aggregation compared to P(PzDPP-Dz) (see Figure S8 for a detailed discussion, Supporting Information). To gain further understanding of the aggregation behavior and backbone planarity, photoluminescence (PL) spectra of the two polymers in CN solutions were measured (Figures 2c and S9 and Supporting Information). The two polymers exhibited different relative intensities of emission peaks between aggregates and single polymer chains (see Figure S9 for a detailed discussion). What is more, the Stokes shift of P(PzDPP-Pz) (0.108 eV) is smaller than that of P(PzDPP-Dz) (0.128 eV). These results indicate that P(PzDPP-Pz) seems to have a stronger aggregation ability and a more planar backbone in comparison to P(PzDPP-Dz) in solution.

We further studied the planarity of the polymer backbones by pressure-dependent Raman spectroscopy (Figure 2e and Section 5, Supporting Information). According to previous studies, if there were some torsional angles in the solid state, the backbone could be planarized by applying hydrostatic pressure of a few gigapascals.[7,39] As shown in Figure 2e, the Raman intensity ratios of P(PzDPP-Pz) are slightly pressure-dependent as the pressure increased from 0 to 2.7 GPa, while the ratios of P(PzDPP-Dz) increased dramatically. These results appear to contradict the DFT studies that showed that P(PzDPP-Dz) has a higher dihedral angle potential. However, MD studies will later show that P(PzDPP-Dz) is poorly packed in the crystalline region, while P(PzDPP-Pz) is closely ordered packed.

To further explore the polymer aggregation behaviors in solution, SANS was performed for both polymers in deuterated 1,2-dichlorobenzene (o-DCB) at 25 °C (Figure 2d, and Section 6, Supporting Information). The Porod exponent provides geometrical information on the polymer aggregates. The Porod exponent of P(PzDPP-Pz) is close to 1, illustrating that the polymer aggregates have a 1D rod-like structure with rigid aggregates. The Porod exponent of P(PzDPP-Dz) is larger than P(PzDPP-Pz), but still much less than 2, suggesting that P(PzDPP-Dz) aggregates still adopt a 1D structure.[40] A flexible cylinder model was used to describe both shapes of the conjugated polymer aggregates in solution. The contour length (L_c) and the Kuhn lengths ($2L_p$, L_p represents the persistence length) obtained from the SANS fitting of P(PzDPP-Pz) and P(PzDPP-Dz) aggregates are summarized in Table S2 (Supporting Information). Both polymers exhibit relatively large contour lengths, indicating the formation of extended aggregates in solution. Notably, the Kuhn length of P(PzDPP-Pz) aggregates (98.6 nm) is substantially larger than that of P(PzDPP-Dz) aggregates (35.8 nm), indicating a higher effective stiffness of the P(PzDPP-Pz) aggregates.

Doping and Thermoelectric Properties

Tetrakis(dimethylamino)ethylene (TDAE), a widely used effective n-dopant, was used to dope the polymers to study the electrical conductivities and thermoelectric properties.[41] P(PzDPP-Pz) achieved high electrical conductivities (σ) of up to 60.5 S cm^{-1}, which is one of the highest in n-doped conjugated polymers, after a 60 min exposure in TDAE vapor. Surprisingly, the isomeric polymer P(PzDPP-Dz) only showed low maximal conductivities of 0.15 S cm^{-1} after 15 min doping. Seebeck coefficients (S) of the two doped polymers were also measured under different doping conditions, and the corresponding PFs ($PF = S^2\sigma$) were also calculated (Table 1, Figures 3a,b and S15−S17, Supporting Information). With the extension of doping time, the Seebeck coefficient of P(PzDPP-Pz) decreased gradually from 416 to 84 μV K^{-1}, which can be ascribed to the increased charge carrier concentration. The maximal PF of P(PzDPP-Pz) was obtained by varying the doping time, yielding a high value of 65.6 μW m^{-1} K^{-2}, which ranks among the highest in solution-processable n-doped conjugated polymers. Similarly, the Seebeck coefficients of P(PzDPP-Dz) decreased from 220 to 114 μV K^{-1}, with a maximal PF of only 0.44 μW m^{-1} K^{-2}. The two isomeric polymers with the same chemical composition and similar LUMO energy levels exhibited over 2 orders of magnitude difference in thermoelectric performance. In addition, we also measured the thermal conductivity of P(PzDPP-Pz) (Section 9 and Table S3, Supporting Information). After correction for the electronic contribution, the thermal conductivity was determined to be 0.30 W m^{-1} K^{-1}, indicating that P(PzDPP-Pz) possesses a low thermal conductivity, thus yielding a thermoelectric figure of merit (ZT) of 0.066.

To characterize the doping level of the polymer films, UV−vis−NIR absorption spectroscopy, UPS, and EPR were used. After doping, both polymers exhibited similar absorption bands in the near-infrared region, suggesting that both polymers can be effectively n-doped (Figure 3d, e). The secondary electron cutoff of the P(PzDPP-Pz) UPS shifted 0.11 eV after doping for 60 min, equivalent to an upward shift of its Fermi level by 0.11 eV, which is similar to the shift value of P(PzDPP-Dz) (0.14 eV) (Figure 3c). In the EPR spectroscopy, both P(PzDPP-Pz) and P(PzDPP-Dz) showed a radical signal after being doped for 5 min. When doping for 60 min, the spin density of P(PzDPP-Dz) and P(PzDPP-Pz) increased to 5.45×10^{19} cm^{-3} and 4.65×10^{19} cm^{-3}, respectively. All of these results suggest that both polymers have similar doping levels,

Downloaded from pubs.acs.org/ancac3/article-pdf/20/15/11545/6504759/8/nn5c13008.pdf by PEKING UNIV user on 23 November 2026

https://doi.org/10.1021/acsnano.5c13008
ACS Nano 2026, 20, 11545−11557

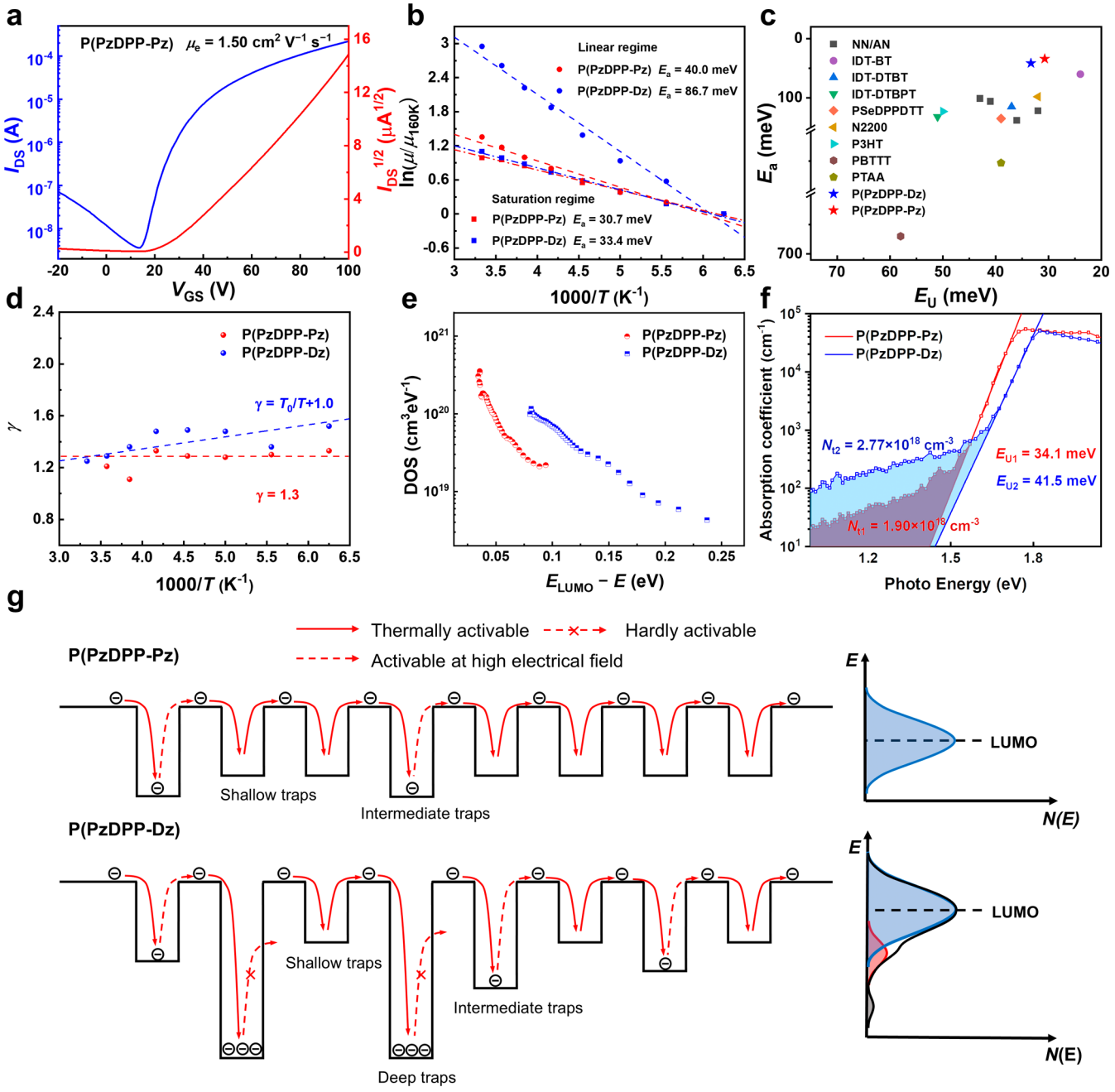


Figure 4. Charge carrier transport properties and energetic disorder evaluation. (a) Transfer characteristics of a P(PzDPP-Pz) FET device in the saturation regime at room temperature. (b) Extracted activation energies from the transfer characteristics at both linear regimes and saturation regimes. (c) Activation energies (saturation regime V_{DS} = 100 V) vs Urbach energies of ours and other reported polymers. (d) γ values versus 1000/T for the polymers. γ was fitted to $I_{DS} \propto (V_{GS} - V_{Th})^{\gamma}$. (e) Comparison of the density of states (DOS) of the polymers, which are calculated based on temperature-dependent OFET measurement. The DOS is plotted as a function of the energy from the LUMO level. (f) Absorption coefficients of both polymer films measured by photothermal deflection spectroscopy (PDS). (g) Schematic illustration of the charge transport properties with different types of traps and their corresponding DOS near the LUMO level of two isomeric polymers.

which cannot account for their significant differences in thermoelectric performance.

The film microstructures of both the pristine and doped P(PzDPP-Pz) and P(PzDPP-Dz) films were characterized by GIWAXS (Figure 3g, h, j, k, and Section 10, Supporting Information). Compared with other D−A conjugated polymers,[42−44] P(PzDPP-Dz) shows relatively weak diffractions, suggesting their films are more amorphous, whereas P(PzDPP-Pz) shows strong (h00) diffractions along the q_z axis. The lamellar packing and π−π stacking distances were calculated to be 29.92 and 3.34 Å for P(PzDPP-Pz) and 29.92 and 3.51 Å for P(PzDPP-Dz) (Table S5 and Supporting Information). After being doped with TDAE, the lamellar and π−π stacking distances of both polymers remain almost unchanged, indicating that dopants do not significantly alter the molecular packings. By using the full width at half-maximum (fwhm) of the (100) diffraction peaks, we found that all the coherence lengths of pristine and doped films show the same trend: P(PzDPP-Pz) > P(PzDPP-Dz) (Figure 3i and Table S5, Supporting Information). The paracrystallinity disorder of

https://doi.org/10.1021/acsnano.5c13008
ACS Nano 2026, 20, 11545−11557

Downloaded from pubs.acs.org/ancac3/article-pdf/20/15/11545/6504759/nn5c13008.pdf by PEKING UNIV user on 23 November 2026

P(PzDPP-Pz) is also lower, indicating that P(PzDPP-Dz) has a higher degree of packing disorder compared with P(PzDPP-Pz) (Figure 3l). Atomic force microscopy (AFM) height images show that both pristine and doped P(PzDPP-Pz) films display fiber-like intercalating networks with larger crystallized zones than P(PzDPP-Dz) (Figure S20, Supporting Information). The pristine films of both P(PzDPP-Pz) and P(PzDPP-Dz) show a smooth morphology with a root-mean-square (RMS) surface roughness of 0.66 and 0.71 nm, respectively. Both doped polymer films remain low roughness (<1 nm), suggesting that doping does not change the film significantly.

Charge Transport Properties and Energetic Disorders Analysis

The electrical conductivity of a material can be calculated using the following equation: $\sigma = q\mu n$, where q is the elementary charge, μ is the charge carrier mobility, and n is the charge carrier concentration. We have demonstrated that after doping, both polymers showed similar charge carrier concentrations. In order to investigate the effect of subtle structure change on the electronic properties, we measured the charge carrier mobilities of the polymers using field-effect transistors (FETs) (Figures 4a and S21 and S22, Supporting Information). Both isomeric polymers display clear n-type transfer characteristics. The electron mobility (μ) was extracted in the saturation regime. Notably, P(PzDPP-Pz) exhibits high electron mobilities of around 1 $cm^2\ V^{-1}\ s^{-1}$, almost 2 orders of magnitude higher than its isomer P(PzDPP-Dz) (0.015 $cm^2\ V^{-1}\ s^{-1}$). We also calculated the effective mobilities (μ_{eff}) of both polymers (see Section 11 in the Supporting Information). The μ_{eff} is 0.71 $cm^2\ V^{-1}\ s^{-1}$ for P(PzDPP-Pz) and 0.007 $cm^2\ V^{-1}\ s^{-1}$ for P(PzDPP-Dz). We also measured the mobilities of the lightly doped polymer films using FETs. The thin polymer films were doped with 2 mol %, 4 mol %, and 6 mol % *N*-DMBI (Figure S23, Supporting Information). After doping, the mobility of the P(PzDPP-Pz) polymer film decreased significantly, which is largely due to the dopant-induced Coulombic traps and molecular packing disorder.[45,46] Surprisingly, the mobilities of P(PzDPP-Dz) increased slightly to 2.29×10^{-2} $cm^2\ V^{-1}\ s^{-1}$ for 2 mol % doping and then decreased to 4.71×10^{-3} $cm^2\ V^{-1}\ s^{-1}$ for 6 mol % doping. The mobility increase is probably due to the trap-filling effect at low doping concentrations.[47,48] Furthermore, AC Hall measurements were performed on the doped polymer thin films (Section 9 and Table S4, Supporting Information). The results show that P(PzDPP-Pz) exhibits a Hall mobility (μ_{Hall}) over 1 order of magnitude higher than that of its isomer P(PzDPP−Dz), while its carrier concentration (n_{Hall}) is also twice higher. These findings consistently confirm that doped P(PzDPP-Pz) possesses a superior charge-transport capability and lower energetic disorder.

To further understand the charge transport properties, temperature-dependent FET measurements (I_{DS} vs V_{GS} from 160 to 300 K) were performed (Figure S24, Supporting Information). Both polymers show small activation energies (E_a) (30.7 meV for P(PzDPP-Pz) and 33.4 meV for P(PzDPP-Dz)) in the saturation regime (V_{DS} = 100 V) (Figure 4b). These values are smaller than all of the conjugated polymers reported to date. This result is unexpected, because P(PzDPP-Dz) has a much lower electron mobility than many of these polymers[7,13,15,49] (Figure 4c and Table S6, Supporting Information). We also measured the E_a values of the polymers in the linear regime (V_{DS} = 20 V). The E_a of P(PzDPP-Pz) slightly increases to 40.0 meV, whereas the E_a of P(PzDPP-Dz) increases largely to 87.0 meV. Thus, P(PzDPP-Dz) exhibits significant voltage-dependent charge transport behaviors. From the current−voltage relationship in a transistor working in the saturation regime, i.e., $I_{DS} \propto (V_{DS} - V_{Th})^{\gamma}$, the exponent γ, which reflects the temperature dependence of the FET device, can be extracted (Figures 4d and S24, Supporting Information). For P(PzDPP-Pz), the exponent γ exhibits a temperature-independent value of nearly 1.3. In contrast, for P(PzDPP-Dz), the exponent γ increases when decreasing the temperature as $\gamma = T_0/T + 1.0$. The increase in exponent γ suggests that the carrier transport in P(PzDPP-Dz) was thermally activated and limited by some trap states. These results are consistent with the activation energy results discussed above.

To determine the DOS of both polymers in the solid state, we further calculated the DOS [$N(E)$] based on the activation energy data at different V_{GS} using Lang's method (see Section 11 and Figure S26, Supporting Information).[50,51] Figure 4e compares the extracted $N(E)$ values of both polymers. The $N(E)$ of P(PzDPP-Dz) varies from 80 to 400 meV, much broader than that of P(PzDPP-Pz) (30 to 100 meV). The band tail of P(PzDPP-Dz) extends deeper into the band gap, suggesting that P(PzDPP-Dz) has more trap states compared with P(PzDPP-Pz). In the following, each DOS spectrum was fitted to a double Gaussian distribution function. The fitting results are shown in Figure S26 and Table S7 (Supporting Information). The Gaussian fitting parameters demonstrated that the DOS of P(PzDPP-Pz) has shallow trap states (E_{peak1} = 19.9 meV) and intermediate trap states (E_{peak1} = 55.9 meV), whereas the trap states (E_{peak1} = 40.0 meV, E_{peak2} = 170 meV) of P(PzDPP-Dz) are located at deeper energy levels and show wider Gaussian distributions.

Apart from electrical measurements, a spectroscopy measurement method, namely, PDS, was also employed (Figure 4f). The PDS method probes subgap optical absorption arising from localized electronic states below the optical band edge, thereby mapping the density and energetic distribution of trap and tail states that reflect intrinsic energetic disorder in organic semiconductors.[52−54] Because PDS is an optical equilibrium technique performed without external bias or carrier injection, it reveals only the static energetic landscape of a material and cannot directly capture the dynamic traps during charge transport. In the PDS, the characteristic width of the exponential absorption tail called, Urbach energy (E_u), has been shown to correlate with the number of energetic disorders and trap states in the band gap.[7] P(PzDPP-Pz) has a sharper bandtail (E_u = 34 meV) while P(PzDPP-Dz) has a wider one (E_u = 42 meV), suggesting that P(PzDPP-Pz) has smaller energetic disorders and less shallow traps. Using PDS, the nominal density of trap states, N_t, of the polymer films can also be estimated (see the detailed estimation procedure in Section 12, Supporting Information). N_t reflects the relatively deeper trap states located in the sub-bandgap region, which has been widely used in understanding the trap states in both inorganic and organic semiconductors.[52,55] The N_t of P(PzDPP-Dz) (2.77×10^{18} cm^{-3}) is larger than that of P(PzDPP-Pz) (1.90×10^{18} cm^{-3}). PDS provides a complementary perspective—quantifying intrinsic static disorder, while FET activation energy studies validate how these energetic features govern real charge transport—together establishing a coherent link among molecular structure, energetic disorder, and mobility.

Downloaded from pubs.acs.org/ancac3/article-pdf/20/15/11545/6504759/nn5c13008.pdf by PEKING UNIV user on 23 November 2026

https://doi.org/10.1021/acsnano.5c13008
ACS Nano 2026, 20, 11545−11557

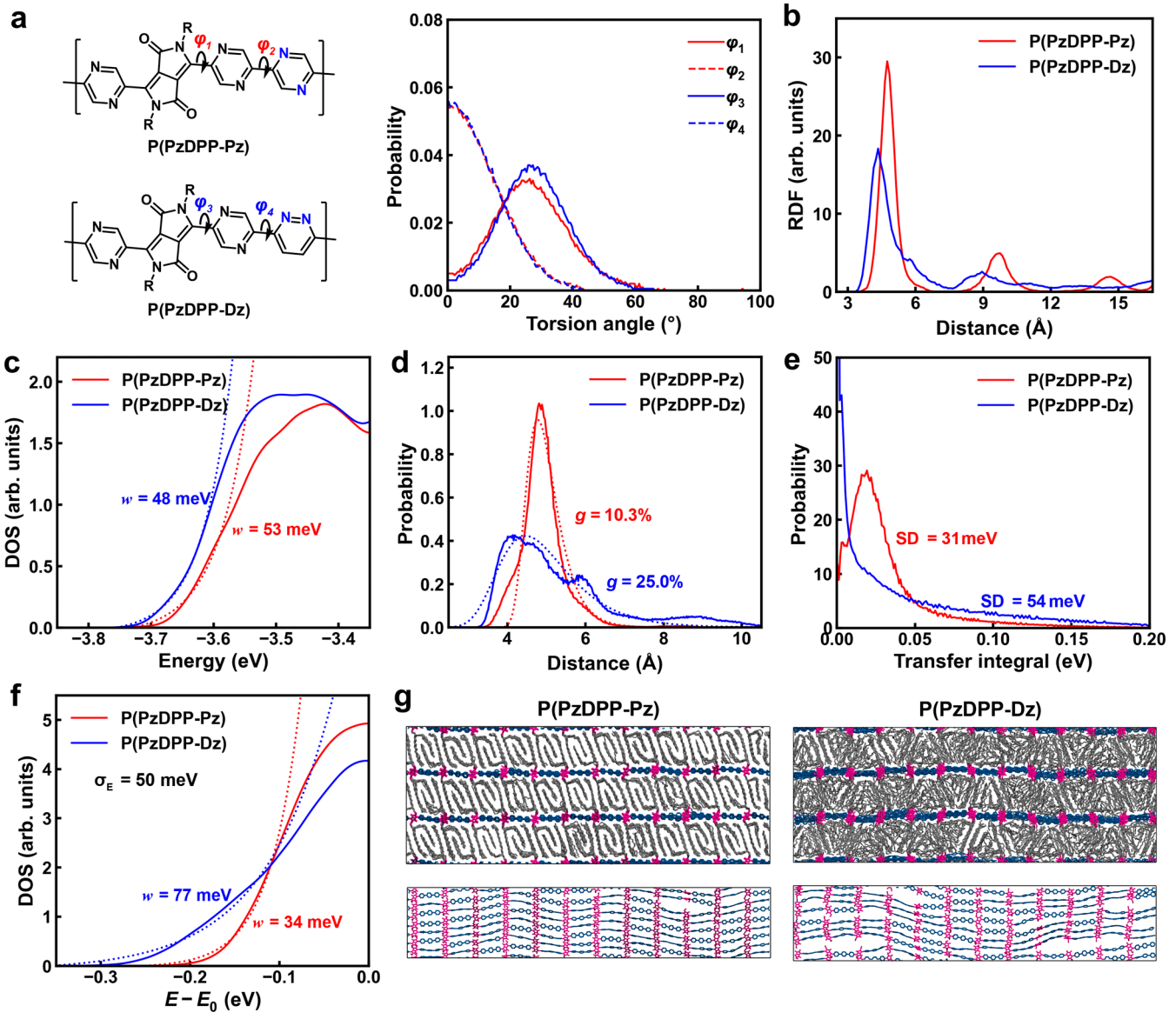


Figure 5. Computational studies to understand the origin of different types of energetic disorders and traps from nanoscale polymer packing. (a) Distributions of dihedral angles along the polymer backbone (φ_1 to φ_4) in the two polymers, extracted from equilibrium MD simulations. (b) RDF between conjugated rings in the crystalline packing structures. (c, f) Calculated intrachain (c) and overall (f) DOS distributions. Dotted lines represent exponential fits to the DOS tails. (d) Distributions of $\pi-\pi$ stacking distances (solid lines) and paracrystallinity parameters estimated via Gumbel function fitting (dotted lines). (e) Distributions of transfer integrals extracted from crystalline structures, along with their standard deviations. (g) MD simulation snapshots in the crystalline regions. For clarity, only one lamella is shown in the side view (bottom), with side chains omitted. Hydrogen atoms are omitted in all images.

Based on the above results, we propose that the two polymers could have different types of traps (or energetic disorders) in the solid state, namely, shallow traps (ca. 20−40 meV), intermediate traps (ca. 40−100 meV), and deep traps (>100 meV) (Figure 4g). For shallow traps, the charged carrier can be thermally activated at room temperature (k_BT = 25.7 meV at 298 K, k_B: Boltzmann constant) under low electrical fields (e.g., in the linear regime, V_{DS} = 20 V). For intermediate traps, the charged carriers can be thermally activated at higher electrical fields (e.g., in the saturation regime, V_{DS} = 100 V). For deep traps, the charged carriers are completely trapped and cannot move. For P(PzDPP-Pz), the major traps come from shallow traps and show very close E_a in both linear and saturation regimes. Thus, the polymer exhibits gate-voltage-independent mobility and a near disorder-free transport behavior. However, for P(PzDPP-Dz), it contains similar shallow traps with an E_a around 30−40 meV, but a large amount of intermediate and deep traps. The intermediate traps can engage in charge transport under high electrical fields, but the large number of deep traps in P(PzDPP-Dz) makes the polymer show very low charge carrier mobilities, even though it has a very rigid backbone and small Urbach energy. Because some deep traps can be filled after doping, P(PzDPP-Dz) shows higher charged carrier mobilities after light doping. These results indicate that the subtle chemical structure differences between the two polymers result in huge traps or energetic disorder differences, which have not previously been observed in the literature.

https://doi.org/10.1021/acsnano.5c13008
ACS Nano 2026, 20, 11545−11557

Downloaded from pubs.acs.org/ancac3/article-pdf/20/15/11545/6504759/nn5c13008.pdf by PEKING UNIV user on 23 November 2026

Understanding of the Nanoscale Polymer Packing

The nanoscale molecular arrangement in the crystalline domains is crucial to charge transport. Crystalline areas with longer conjugation lengths and stronger interchain interactions enable effective interchain charge transport, whereas amorphous regions contribute less. Therefore, it is essential to model the crystalline regions and their nanoscale molecular packing. To explore the impact of the microstructural arrangement of the crystalline regions on energy disorder and performance, we performed atomistic MD simulations using the GROMACS software package[56] (See details in Section 14, Supporting Information). The general AMBER force field and restrained electrostatic potential atomic charges were applied to describe bonding and nonbonding interactions. A series of MD simulations, extending up to 35 ns, allowed us to obtain stable crystalline arrangements of the two rigid polymer backbone structures (Figure S30).

From the equilibrium crystalline structures (Figure 5g), P(PzDPP-Pz) exhibits a more ordered structure than that of P(PzDPP-Dz). The side chains of P(PzDPP-Pz) demonstrate a well-organized interdigitation, while those of P(PzDPP-Dz) are relatively disordered and entangled. The arrangement of the side chains in both polymers is clearly correlated with the degree of interchain $\pi-\pi$ stacking order. The radial distribution function (RDF) of the conjugated rings in P(PzDPP-Pz) displays peaks significantly sharper than that of P(PzDPP-Dz) (Figure 5b), indicating a lower degree of disorder. Dihedral angle fluctuations along the polymer backbone have recently been identified as a primary source of energetic disorder in charge transport.[7,8] In both polymers, there are two key dihedral angles: within PzDPP (φ_1 and φ_3), and between PzDPP and Pz/Dz (φ_2 and φ_4) (Figure 5a). Notably, the distribution of dihedral angles in crystalline P(PzDPP-Pz) is similar to that in P(PzDPP-Dz) (Figure 5b), despite DFT calculations demonstrating higher torsional barriers in P(PzDPP-Dz) (Figure S28). These findings suggest that following the stacking of polymer molecules into a crystalline arrangement, the structure of the polymer backbone influences the three-dimensional microstructural packing, including $\pi-\pi$ stacking distances and side chain orientations, with P(PzDPP-Pz) being significantly more ordered. This also underscores the important insight that, when evaluating energetic disorder, the nanoscale polymer packing structure must be carefully considered.

The electronic DOS distribution and energetic disorder were further calculated using MD snapshots (Section 14, Supporting Information). First, we extracted 500 snapshots from the 10 ns production run and randomly selected 500 polymer chains to calculate the orbital energies from LUMO to LUMO + 11 for each polymer chain. These orbital energies were then combined to construct the overall DOS distribution for the entire polymer system. The resulting DOS distributions show only minor differences in the characteristic trap state depth (w) between the two polymers (Figures S31 and 5c), suggesting that the energetic disorder originating from intrachain conformations is minimal. In the aforementioned calculations of the intrachain DOS distributions, we considered only the electronic states localized on individual polymer chains without accounting for the interchain electronic coupling of the packing structures.

To further explore the contribution of nanoscale polymer packing, we calculated the distribution of $\pi-\pi$ stacking distances in the crystalline region and the interchain coupling distribution. We observed that P(PzDPP-Pz) exhibits a lower degree of paracrystallinity ($g_{P(PzDPP-Pz)}$ = 10.3%, $g_{P(PzDPP-Dz)}$ = 25.0%), partially indicating a more orderly arrangement of its crystalline regions (Figure 5d). Previous studies have suggested that paracrystalline disorder is a determinant of energetic disorder in semicrystalline polymers by broadening the DOS tail.[57] To quantify interchain energetic disorder, we constructed a simplified one-dimensional tight-binding model (see Figure S32 and Section 14, Supporting Information). The resulting DOS is shown in Figure 5f. The DOS tail was fitted to the exponential function to extract the overall energetic disorder w. Taking interchain energetic disorder into account, the extracted DOS tail depth of P(PzDPP-Pz) (w = 34 meV) is less than half that of P(PzDPP-Dz) (w = 77 meV) (Figure 5f). This result aligns well with the GIWAXS and variable-temperature OFET E_a results. Therefore, we can conclude that the primary reason for the observed differences in energy disorder and performances between the two polymers is variations in the three-dimensional nanoscale polymer packing rather than differences in the intrinsic rigidity of the polymer backbone itself.

CONCLUSIONS

In summary, we designed and synthesized two isomeric conjugated polymers to investigate the origins of energetic disorders and their relationship with nanoscale polymer packing structures. Despite minor differences in their chemical structures, these polymers exhibited significant disparities in charge transport and thermoelectric (TE) properties. Our comprehensive analysis revealed that conjugated polymer films can encompass various types of energetic disorders and traps across multilevel nanoscale structures in the solid state. Our findings underscore the essential role of the nanoscale packing structures of polymers in determining charge transport properties. Based on this work, we believe the following guidelines can be concluded for future polymer TE materials design: (i) While rigid backbone conformation helps reduce energetic disorder and enhance charge transport, nanoscale polymer packing plays an equally important role. Carefully optimizing polymer packing either by molecular design or by a fabrication process is necessary. (ii) Our results highlight the significance of side chain orientations and arrangements in determining energetic disorders. Thus, strategically tuning the types, branching positions, and lengths could be useful. For example, hydrogen bonding could be introduced to the side chain to tune nanoscale polymer packing and reduce packing-induced disorders. (iii) Some fabrication methods (e.g., solution shearing), which enable tuning of polymer nanoscale structures and induce polymer chain alignment,[58] could lead to further reduced energetic disorders and enhanced charge transport.

EXPERIMENTAL SECTION

Polymer Synthesis and Characterization

Synthesis of P(PzDPP-Pz): A 50 mL Schlenk tube was added PzDPP-2Br monomer (53.91 mg, 0.040 mmol), 2,5-bis(tributylstannyl)-pyrazine monomer (26.33 mg, 0.040 mmol), $Pd(PPh_3)_4$ (1.85 mg, 4 mol %), CuI (0.61 mg, 8 mol %), 7.2 mL anhydrous toluene, and 0.8 mL anhydrous NMP. The tube was placed in liquid nitrogen to freeze the solution and then evacuated. This procedure was repeated three times. The sealed tube was heated to 110 °C and stirred for 36 h. After the reaction mixture was cooled to room temperature, *N*,*N*′-diethylphenylazothioformamide (3 mg, 0.014 mmol) was added, and

Downloaded from pubs.acs.org/ancac3/article-pdf/20/15/11545/6504759/8/nn5c13008.pdf by PEKING UNIV user on 23 November 2026

https://doi.org/10.1021/acsnano.5c13008
ACS Nano 2026, 20, 11545−11557

the resulting mixture was stirred at 80 °C for 30 min. The reaction mixture was poured into 200 mL methanol to precipitate the polymer, which was filtered and the solid was placed in a Soxhlet extractor and extracted successively with methanol, acetone, hexane, tetrahydrofuran, dichloromethane, chloroform, and chlorobenzene. The chlorobenzene solution was concentrated under reduced pressure, and the concentrated solution was poured into 200 mL of methanol to precipitate the polymer. The suspension was filtered and dried in vacuum to afford P(PzDPP-Pz) as a dark blue solid (35 mg, 69%). Detailed synthetic routes and characterization data are shown in Supporting Information.

Synthesis of P(PzDPP-Dz): A 50 mL Schlenk tube was added PzDPP-2Br monomer (53.91 mg, 0.040 mmol), 3,6-bis-(tributylstannyl)pyridazine monomer (26.33 mg, 0.040 mmol), $Pd(PPh_3)_4$ (1.85 mg, 4 mol %), CuI (0.61 mg, 8 mol %), 7.2 mL anhydrous toluene, and 0.8 mL anhydrous NMP. The tube was placed in liquid nitrogen to freeze the solution and then evacuated. This procedure was repeated three times. The sealed tube was heated to 110 °C and stirred for 36 h. After the reaction mixture was cooled to room temperature, *N,N′*-diethylphenylazothioformamide (3 mg, 0.014 mmol) was added, and the resulting mixture was stirred at 80 °C for 30 min. Then the reaction mixture was poured into 200 mL of methanol to precipitate the polymer, which was filtered, and the solid was placed in a Soxhlet extractor and extracted successively with methanol, acetone, hexane, tetrahydrofuran, dichloromethane, chloroform, chlorobenzene, and 1,1,2,2-tetrachloroethane. The 1,1,2,2-tetrachloroethane solution was concentrated under reduced pressure, and the concentrated solution was poured into 200 mL of methanol to precipitate the polymer. The suspension was filtered and dried under vacuum to afford P(PzDPP-Dz) as a dark blue solid (41 mg, 81%). Detailed synthetic routes and characterization data are shown in Supporting Information.

Field Effect Transistor Device Fabrication and Characterization

FET devices with top-gate/bottom-contact configurations were fabricated to characterize the charge carrier mobilities of the polymers. Source and drain electrodes (Ti 2 nm/Au 40 nm) were patterned on a SiO_2 substrate by photolithography and lift-off process. The substrates were cleaned by using ultrasonication in acetone, cleaning agent, deionized water (three times), and isopropanol. A thin polymer film was deposited using a two-step spin-coating process at 1500 rpm for 60 s and 3000 rpm for 3 s using the polymer solution of 3 g/L in 1-chloronaphthalene (1-CN). The polymer film was first baked at 100 °C for 3 min and then annealed at 150 °C for 10 min. After the polymer film was deposited, a CYTOP solution (CTL809M/CT-solv 180 = 3/1) was spin-coated on top of the polymer film at 2000 rpm for 60 s and then annealed at 100 °C for 10 min to yield a dielectric layer of 500 nm thickness. An aluminum layer of 50 nm was then evaporated on the dielectric layer as the gate electrode. The optimized channel length of OFETs for both polymers is L = 10 μm, with a channel width-to-length ratio of W/L = 20, W = 200 μm. For the electrical measurements, the saturation-regime characteristics were measured at V_{DS} = 100 V, while the linear-regime characteristics were recorded at V_{DS} = 20 V. All other relevant measurement parameters are now explicitly indicated in the corresponding figures. The FET devices were measured on a probe stage under nitrogen in the glovebox using a Keithley 4200 SCS Parameter Analyzer.

Thermoelectric Device Fabrication and Characterization

The thermoelectric properties of the doped P(PzDPP-Pz) and P(PzDPP-Dz) films were studied in the glovebox to avoid temperature fluctuation and the dedoping of the O_2/water. The electrodes (Ti 2 nm/Au 40 nm) (L = 200 μm, W/L = 5) were patterned on the glass substrates by using photolithography and a lift-off process.

The Seebeck coefficient (S) was calculated by $S = \Delta V_{therm}/\Delta T$, where ΔV_{therm} is the thermal voltage between the hot and cold ends of the device upon temperature gradient ΔT. The ΔV_{therm} was monitored by Keithley 4200 SCS, and the temperature difference was introduced by a Joule heat (heater) and liquid nitrogen cooling system. To precisely determine the temperature difference ΔT between the two contact pads, two temperature-sensing wires (5 nm Cr/20 nm Au bilayer) were placed on the hot and cold ends of the patterned polymer layer. The temperature coefficient of resistance (TCR) of the temperature-sensing wires was calculated from the slope of the measured resistance versus temperature. The resistance of the metal wires is linearly correlated with the temperature. The TCR was found to be 0.307 Ω K^{-1} with R^2 = 0.9999. By monitoring the resistance evolution of the temperature-sensing electrodes, the accurate temperature of the contact pads was figured out by $T_h = T_{r.t.} + (R_h - R_{r.t.})/\mathrm{TCR}$ and $T_c = T_{r.t.} + (R_c - R_{r.t.})/\mathrm{TCR}$, where T_h and T_c are the hot and cold pad temperatures, R_h and R_c are the measured resistances, and $T_{r.t.}$ and $R_{r.t.}$ are the room temperature and resistance values, respectively. The temperature difference was then known as the difference in temperature between the hot and cold ends, $\Delta T = T_h - T_c$.

Electrical conductivity (σ) was measured by a linear four-probe method and calculated using the equation $\sigma = L/(R \times A) = L/(R \times W \times t)$, where R = U/I and W/L = 5. The voltage (U) and current (I) were monitored by a Keithley 4200 SCS, and the film thickness (t) was measured using AFM.

The device configuration used for measuring both electrical conductivity and the Seebeck coefficient is illustrated in Figure S15. Electrical conductivity was measured with a colinear four-probe bar geometry (D = 0.1 mm, L = 0.1 mm, W/L = 5). For the Seebeck measurement, the electrical contacts were bars of 0.1 × 0.5 mm, placed 5 mm apart to establish the temperature gradient ΔT.

■ ASSOCIATED CONTENT

Supporting Information

The Supporting Information is available free of charge at https://pubs.acs.org/doi/10.1021/acsnano.5c13008.

General procedures and experimental details; polymer building block combinations screening process; DFT calculations for the evaluation of polymer building block planarity; characterization of molecular weights, thermal properties, and CV of the polymers; optical spectroscopy and characterization; SANS characterization; doping and thermoelectric devices; Seebeck coefficient measurement of doped polymer films; thermal conductivity and AC Hall measurements for doped polymer films; microstructure characterization of the pristine and TDAE-doped polymers; charge transfer properties characterization based on FET devices; PDS; time-dependent decay of the electrical conductivity; MD simulations and DOS calculations; and synthetic routes of the new compounds(PDF)

■ AUTHOR INFORMATION

Corresponding Authors

Guangchao Liu − *State Key Laboratory of Advanced Waterproof Materials, School of Materials Science and Engineering, Peking University, Beijing 100871, China;* orcid.org/0009-0004-4811-5138; Email: gcliu@pku.edu.cn

Dong Wang − *State Key Laboratory of Flexible Electronics Technology, Tsinghua University, Beijing 100084, China;* Email: dong913@tsinghua.edu.cn

Zhi Zhang − *State Key Laboratory of Advanced Waterproof Materials, School of Materials Science and Engineering, Peking University, Beijing 100871, China;* Email: zhizhang@pku.edu.cn

Downloaded from pubs.acs.org/ancac3/article-pdf/20/15/11545/6504759/8/nn5c13008.pdf by PEKING UNIV user on 23 November 2026

Ting Lei − *State Key Laboratory of Advanced Waterproof Materials, School of Materials Science and Engineering, Peking University, Beijing 100871, China;* orcid.org/0000-0001-8190-9483; Email: tinglei@pku.edu.cn

Authors

Jia-Tong Li − *State Key Laboratory of Advanced Waterproof Materials, School of Materials Science and Engineering, Peking University, Beijing 100871, China*

Chunlin Xu − *State Key Laboratory of Flexible Electronics Technology and MOE Key Laboratory of Organic OptoElectronics and Molecular Engineering, Department of Chemistry, Tsinghua University, Beijing 100084, China;* orcid.org/0000-0003-4309-2307

Juan-Rong Wang − *State Key Laboratory of Advanced Waterproof Materials, School of Materials Science and Engineering, Peking University, Beijing 100871, China*

Zhuoqiong Zhang − *Department of Physics, Institute of Advanced Materials, Hong Kong Baptist University, Kowloon Tong, Hong Kong SAR 999077, China;* orcid.org/0000-0003-3121-9948

Yunfei Wang − *School of Polymer Science and Engineering, Center for Optoelectronic Materials and Devices, The University of Southern Mississippi, Hattiesburg, Mississippi 39406, United States;* orcid.org/0000-0001-7555-5308

Zhiqiang Cao − *School of Polymer Science and Engineering, Center for Optoelectronic Materials and Devices, The University of Southern Mississippi, Hattiesburg, Mississippi 39406, United States*

Yin Liang − *State Key Laboratory of Advanced Waterproof Materials, School of Materials Science and Engineering, Peking University, Beijing 100871, China*

Xin-Yu Deng − *State Key Laboratory of Advanced Waterproof Materials, School of Materials Science and Engineering, Peking University, Beijing 100871, China;* orcid.org/0000-0002-9249-1411

Miao Xiong − *State Key Laboratory of Advanced Waterproof Materials, School of Materials Science and Engineering, Peking University, Beijing 100871, China; Beijing National Laboratory for Molecular Science, College of Chemistry and Molecular Engineering, Peking University, Beijing 100871, China*

Xue-Qing Wang − *State Key Laboratory of Advanced Waterproof Materials, School of Materials Science and Engineering, Peking University, Beijing 100871, China*

Kai-Kai Liu − *State Key Laboratory of Advanced Waterproof Materials, School of Materials Science and Engineering, Peking University, Beijing 100871, China*

Qing Zhang − *State Key Laboratory of Advanced Waterproof Materials, School of Materials Science and Engineering, Peking University, Beijing 100871, China;* orcid.org/0000-0002-6869-0381

Xiaodan Gu − *School of Polymer Science and Engineering, Center for Optoelectronic Materials and Devices, The University of Southern Mississippi, Hattiesburg, Mississippi 39406, United States;* orcid.org/0000-0002-1123-3673

Shu Kong So − *Department of Physics, Institute of Advanced Materials, Hong Kong Baptist University, Kowloon Tong, Hong Kong SAR 999077, China*

Chuan-Ding Dong − *Department of Physics and Center for Optoelectronics and Photonics Paderborn (CeOPP), Paderborn University, 33098 Paderborn, Germany;* orcid.org/0000-0001-8438-4416

Kai Lin Woon − *Low Dimensional Material Research Center, Department of Physics, Universiti Malaya, 50603 Kuala Lumpur, Malaysia;* orcid.org/0000-0002-2037-8313

Complete contact information is available at: https://pubs.acs.org/10.1021/acsnano.5c13008

Author Contributions

[▽]J.-T.L., G.L., and C.X. contributed equally to this work. The manuscript was written through the contributions of all authors. All authors have given approval to the final version of the manuscript.

Notes

The authors declare no competing financial interest.

■ ACKNOWLEDGMENTS

This work is supported by the National Natural Science Foundation of China (T2425010, T2521001, and 52403219). G.L. thanks the support from the China Postdoctoral Science Foundation (2020M680232). X.G., Y.W., and C.Z. gratefully acknowledge support from the U.S. Department of Energy, Office of Basic Energy Sciences, for the X-ray and neutron scattering work through Grant No. DE-SC0022050. We acknowledge the Molecular Materials and Nanofabrication Laboratory, the Materials Processing and Analysis Center, and the Electron Microscopy Laboratory of Peking University for instrument use. The computational part is supported by the High-performance Computing Platform of Peking University and Center of High Performance Computing at Tsinghua University. This research used resources at the Spallation Neutron Source, a DOE Office of Science User Facility operated by the Oak Ridge National Laboratory. The beam time was allocated to EQ-SANS on proposal number IPTS-28394.1.

■ REFERENCES

(1) Russ, B.; Glaudell, A.; Urban, J. J.; Chabinyc, M. L.; Segalman, R. A. Organic Thermoelectric Materials for Energy Harvesting and Temperature Control. *Nat. Rev. Mater.* **2016**, *1*, 16050.

(2) Zhang, Z.; Wang, W.; Jiang, Y.; Wang, Y.-X.; Wu, Y.; Lai, J.-C.; Niu, S.; Xu, C.; Shih, C.-C.; Wang, C.; Yan, H.; Galuska, L.; Prine, N.; Wu, H.-C.; Zhong, D.; Chen, G.; Matsuhisa, N.; Zheng, Y.; Yu, Z.; Wang, Y.; Dauskardt, R.; Gu, X.; Tok, J. B.-H.; Bao, Z. High-Brightness All-Polymer Stretchable LED with Charge-Trapping Dilution. *Nature* **2022**, *603*, 624−630.

(3) Lopez, J.; Mackanic, D. G.; Cui, Y.; Bao, Z. Designing Polymers for Advanced Battery Chemistries. *Nat. Rev. Mater.* **2019**, *4*, 312−330.

(4) Dou, L.; Liu, Y.; Hong, Z.; Li, G.; Yang, Y. Low-Bandgap Near-IR Conjugated Polymers/Molecules for Organic Electronics. *Chem. Rev.* **2015**, *115*, 12633−12665.

(5) Fornari, R. P.; Blom, P. W. M.; Troisi, A. How Many Parameters Actually Affect the Mobility of Conjugated Polymers? *Phys. Rev. Lett.* **2017**, *118*, 086601.

(6) Fratini, S.; Nikolka, M.; Salleo, A.; Schweicher, G.; Sirringhaus, H. Charge Transport in High-Mobility Conjugated Polymers and Molecular Semiconductors. *Nat. Mater.* **2020**, *19*, 491−502.

(7) Venkateshvaran, D.; Nikolka, M.; Sadhanala, A.; Lemaur, V.; Zelazny, M.; Kepa, M.; Hurhangee, M.; Kronemeijer, A. J.; Pecunia, V.; Nasrallah, I.; Romanov, I.; Broch, K.; McCulloch, I.; Emin, D.; Olivier, Y.; Cornil, J.; Beljonne, D.; Sirringhaus, H. Approaching Disorder-Free Transport in High-Mobility Conjugated Polymers. *Nature* **2014**, *515*, 384−388.

(8) Yan, X.; Xiong, M.; Deng, X.-Y.; Liu, K.-K.; Li, J.-T.; Wang, X.-Q.; Zhang, S.; Prine, N.; Zhang, Z.; Huang, W.; Wang, Y.; Wang, J.-Y.;

Downloaded from pubs.acs.org/ancac3/article-pdf/20/15/11545/6504759/nn5c13008.pdf by PEKING UNIV user on 23 November 2026

Gu, X.; So, S. K.; Zhu, J.; Lei, T. Approaching Disorder-Tolerant Semiconducting Polymers. *Nat. Commun.* **2021**, *12*, 5723.
(9) Xiong, M.; Deng, X.-Y.; Tian, S.-Y.; Liu, K.-K.; Fang, Y.-H.; Wang, J.-R.; Wang, Y.; Liu, G.; Chen, J.; Villalva, D. R.; Baran, D.; Gu, X.; Lei, T. Counterion Docking: a General Approach to Reducing Energetic Disorder in Doped Polymeric Semiconductors. *Nat. Commun.* **2024**, *15*, 4972.
(10) Ding, L.; Yu, Z.-D.; Wang, X.-Y.; Yao, Z.-F.; Lu, Y.; Yang, C.-Y.; Wang, J.-Y.; Pei, J. Polymer Semiconductors: Synthesis, Processing, and Applications. *Chem. Rev.* **2023**, *123*, 7421−7497.
(11) Chen, H.; Hurhangee, M.; Nikolka, M.; Zhang, W.; Kirkus, M.; Neophytou, M.; Cryer, S. J.; Harkin, D.; Hayoz, P.; Abdi-Jalebi, M.; McNeill, C. R.; Sirringhaus, H.; McCulloch, I. Dithiopheneindenofluorene (TIF) Semiconducting Polymers with Very High Mobility in Field-Effect Transistors. *Adv. Mater.* **2017**, *29*, 1702523.
(12) Chen, H.; Wadsworth, A.; Ma, C.; Nanni, A.; Zhang, W.; Nikolka, M.; Luci, A. M. T.; Perdigao, L. M. A.; Thorley, K. J.; Cendra, C.; Larson, B.; Rumbles, G.; Anthopoulos, T. D.; Salleo, A.; Costantini, G.; Sirringhaus, H.; McCulloch, I. The Effect of Ring Expansion in Thienobenzo[b]indacenodithiophene Polymers for Organic Field-Effect Transistors. *J. Am. Chem. Soc.* **2019**, *141*, 18806−18813.
(13) Nikolka, M.; Hurhangee, M.; Sadhanala, A.; Chen, H.; McCulloch, I.; Sirringhaus, H. Correlation of Disorder and Charge Transport in a Range of Indacenodithiophene-Based Semiconducting Polymers. *Adv. Electron. Mater.* **2018**, *4*, 1700410.
(14) Onwubiko, A.; Yue, W.; Jellett, C.; Xiao, M.; Chen, H. Y.; Ravva, M. K.; Hanifi, D. A.; Knall, A. C.; Purushothaman, B.; Nikolka, M.; Flores, J. C.; Salleo, A.; Bredas, J.-L.; Sirringhaus, H.; Hayoz, P.; McCulloch, I. Fused Electron Deficient Semiconducting Polymers for Air Stable Electron Transport. *Nat. Commun.* **2018**, *9*, 416.
(15) Xiao, M.; Carey, R. L.; Chen, H.; Jiao, X.; Lemaur, V.; Schott, S.; Nikolka, M.; Jellett, C.; Sadhanala, A.; Rogers, S.; Senanayak, S. P.; Onwubiko, A.; Han, S.; Zhang, Z.; Abdi-Jalebi, M.; Zhang, Y.; Thomas, T. H.; Mahmoudi, N.; Lai, L.; Selezneva, E.; Ren, X.; Nguyen, M.; Wang, Q.; Jacobs, I.; Yue, W.; McNeill, C. R.; Liu, G.; Beljonne, D.; McCulloch, I.; Sirringhaus, H. Charge Transport Physics of a Unique Class of Rigid-Rod Conjugated Polymers with Fused-Ring Conjugated Units Linked by Double Carbon-Carbon Bonds. *Sci. Adv.* **2021**, *7*, No. eabe5280.
(16) Cao, Z.; Leng, M.; Cao, Y.; Gu, X.; Fang, L. How Rigid Are Conjugated Non-Ladder and Ladder Polymers? *J. Polym. Sci.* **2022**, *60*, 298−310.
(17) Li, J.-L.; Deng, X.-Y.; Chen, J.; Fu, P.-X.; Tian, S.-Y.; Wang, Y.; Gu, X.; Lei, T. Cationic Conjugated Polymers with Enhanced Doped-State Planarity for N-Type Organic Thermoelectrics. *CCS Chem.* **2025**, *7*, 1449−1458.
(18) Chen, H.; Moser, M.; Wang, S.; Jellett, C.; Thorley, K.; Harrison, G. T.; Jiao, X.; Xiao, M.; Purushothaman, B.; Alsufyani, M.; Bristow, H.; De Wolf, S.; Gasparini, N.; Wadsworth, A.; McNeill, C. R.; Sirringhaus, H.; Fabiano, S.; McCulloch, I. Acene Ring Size Optimization in Fused Lactam Polymers Enabling High N-Type Organic Thermoelectric Performance. *J. Am. Chem. Soc.* **2021**, *143*, 260−268.
(19) Huang, H.; Chen, Z.; Ortiz, R. P.; Newman, C.; Usta, H.; Lou, S.; Youn, J.; Noh, Y.-Y.; Baeg, K.-J.; Chen, L. X.; Facchetti, A.; Marks, T. Combining Electron-Neutral Building Blocks with Intramolecular "Conformational Locks" Affords Stable, High-Mobility P- and N-Channel Polymer Semiconductors. *J. Am. Chem. Soc.* **2012**, *134*, 10966−10973.
(20) Huang, H.; Yang, L.; Facchetti, A.; Marks, T. J. Organic and Polymeric Semiconductors Enhanced by Noncovalent Conformational Locks. *Chem. Rev.* **2017**, *117*, 10291−10318.
(21) Jackson, N. E.; Savoie, B. M.; Kohlstedt, K. L.; Olvera de la Cruz, M.; Schatz, G. C.; Chen, L. X.; Ratner, M. A. Controlling Conformations of Conjugated Polymers and Small Molecules: the Role of Nonbonding Interactions. *J. Am. Chem. Soc.* **2013**, *135*, 10475−10483.
(22) Yan, X.; Xiong, M.; Li, J.-T.; Zhang, S.; Chase, Z. A.; Lu, Y.; Wang, Z.-Y.; Yao, Z.-F.; Wang, J.-Y.; Gu, X.; Lei, T. Pyrazine-Flanked Diketopyrrolopyrrole (DPP): A New Polymer Building Block for High-Performance N-Type Organic Thermoelectrics. *J. Am. Chem. Soc.* **2019**, *141*, 20215−20221.
(23) Tam, T. L. D.; Xu, J. Strategies and Concepts in N-Doped Conjugated Polymer Thermoelectrics. *J. Mater. Chem. A* **2021**, *9*, 5149−5163.
(24) Qu, D.; Qi, T.; Huang, H. Acceptor−Acceptor-Type Conjugated Polymer Semiconductors. *J. Energy Chem.* **2021**, *59*, 364−387.
(25) Lee, S.; Kim, S.; Pathak, A.; Tripathi, A.; Qiao, T.; Lee, Y.; Lee, H.; Woo, H. Y. Recent Progress in Organic Thermoelectric Materials and Devices. *Macromol. Res.* **2020**, *28*, 531−552.
(26) Sun, H.; Guo, X.; Facchetti, A. High-Performance N-Type Polymer Semiconductors: Applications, Recent Development, and Challenges. *Chem* **2020**, *6*, 1310−1326.
(27) Lu, Y.; Wang, J.-Y.; Pei, J. Strategies To Enhance the Conductivity of N-Type Polymer Thermoelectric Materials. *Chem. Mater.* **2019**, *31*, 6412−6423.
(28) Plé, N.; Turck, A.; Heynderickx, A.; Quéguiner, G. Functionalization by Metallation of Fluoropyrazine. Diazines XXI. *Tetrahedron* **1998**, *54*, 4899−4912.
(29) Huang, K.; Rhys, A. Theory of Light Absorption and Non-Radiative Transitions in *F*-centres. *Proc. R. Soc. London, Ser. A* **1950**, *204*, 406−423.
(30) Cannizzo, A.; van Mourik, F.; Gawelda, W.; Zgrablic, G.; Bressler, C.; Chergui, M. Broadband Femtosecond Fluorescence Spectroscopy of $[Ru(bpy)_3]_2^+$. *Angew. Chem. Int. Ed.* **2006**, *45*, 3174−3176.
(31) Raithel, D.; Baderschneider, S.; de Queiroz, T. B.; Lohwasser, R.; Köhler, J.; Thelakkat, M.; Kümmel, S.; Hildner, R. Emitting Species of Poly(3-hexylthiophene): From Single, Isolated Chains to Bulk. *Macromolecules* **2016**, *49*, 9553−9560.
(32) Raithel, D.; Simine, L.; Pickel, S.; Schotz, K.; Panzer, F.; Baderschneider, S.; Schiefer, D.; Lohwasser, R.; Kohler, J.; Thelakkat, M.; Sommer, M.; Kohler, A.; Rossky, P. J.; Hildner, R. Direct Observation of Backbone Planarization via Side-Chain Alignment in Single Bulky-Substituted Polythiophenes. *Proc. Natl. Acad. Sci. U. S. A* **2018**, *115*, 2699−2704.
(33) Keheze, F. M.; Raithel, D.; Wu, T.; Schiefer, D.; Sommer, M.; Hildner, R.; Reiter, G. Signatures of Melting and Recrystallization of a Bulky Substituted Poly(thiophene) Identified by Optical Spectroscopy. *Macromolecules* **2017**, *50*, 6829−6839.
(34) Ho, P. K. H.; Kim, J.-S.; Tessler, N.; Friend, R. H. Photoluminescence of Poly(p-phenylenevinylene)−Silica Nanocomposites: Evidence for Dual Emission by Franck−Condon Analysis. *J. Chem. Phys.* **2001**, *115*, 2709−2720.
(35) Spano, F. C. Absorption in Regio-Regular Poly(3-hexyl)-thiophene Thin Films: Fermi Resonances, Interband Coupling and Disorder. *Chem. Phys.* **2006**, *325*, 22−35.
(36) Clark, J.; Silva, C.; Friend, R. H.; Spano, F. C. Role of Intermolecular Coupling in the Photophysics of Disordered Organic Semiconductors: Aggregate Emission in Regioregular Polythiophene. *Phys. Rev. Lett.* **2007**, *98*, 206406.
(37) Clark, J.; Chang, J.-F.; Spano, F. C.; Friend, R. H.; Silva, C. Determining Exciton Bandwidth and Film Microstructure in Polythiophene Films Using Linear Absorption Spectroscopy. *Appl. Phys. Lett.* **2009**, *94*, 163306.
(38) de Jong, M.; Seijo, L.; Meijerink, A.; Rabouw, F. T. Resolving the Ambiguity in the Relation Between Stokes Shift and Huang-Rhys Parameter. *Phys. Chem. Chem. Phys.* **2015**, *17*, 16959−16969.
(39) Schmidtke, J. P.; Kim, J.-S.; Gierschner, J.; Silva, C.; Friend, R. H. Optical Spectroscopy of a Polyfluorene Copolymer at High Pressure: Intra- and Intermolecular Interactions. *Phys. Rev. Lett.* **2007**, *99*, 167401.
(40) Zheng, Y.-Q.; Yao, Z.-F.; Lei, T.; Dou, J.-H.; Yang, C.-Y.; Zou, L.; Meng, X.; Ma, W.; Wang, J.-Y.; Pei, J. Unraveling the Solution-State Supramolecular Structures of Donor-Acceptor Polymers and

Downloaded from pubs.acs.org/ancac3/article-pdf/20/15/11545/6504759/8/nn5c13008.pdf by PEKING UNIV user on 23 November 2026

https://doi.org/10.1021/acsnano.5c13008
ACS Nano 2026, 20, 11545−11557

their Influence on Solid-State Morphology and Charge-Transport Properties. *Adv. Mater.* **2017**, *29*, 1701072.
(41) Wang, S.; Sun, H.; Ail, U.; Vagin, M.; Persson, P. O.; Andreasen, J. W.; Thiel, W.; Berggren, M.; Crispin, X.; Fazzi, D.; Fabiano, S. Thermoelectric Properties of Solution-Processed n-Doped Ladder-Type Conducting Polymers. *Adv. Mater.* **2016**, *28*, 10764−10771.
(42) Liu, J.; van der Zee, B.; Alessandri, R.; Sami, S.; Dong, J.; Nugraha, M. I.; Barker, A. J.; Rousseva, S.; Qiu, L.; Qiu, X.; Klasen, N.; Chiechi, R. C.; Baran, D.; Caironi, M.; Anthopoulos, T. D.; Portale, G.; Havenith, R. W. A.; Marrink, S. J.; Hummelen, J. C.; Koster, L. J. A. N-type Organic Thermoelectrics: Demonstration of ZT > 0.3. *Nat. Commun.* **2020**, *11*, 5694.
(43) Lu, Y.; Yu, Z.-D.; Un, H.-I.; Yao, Z.-F.; You, H.-Y.; Jin, W.; Li, L.; Wang, Z.-Y.; Dong, B.-W.; Barlow, S.; Longhi, E.; Di, C.-A.; Zhu, D.; Wang, J.-Y.; Silva, C.; Marder, S. R.; Pei, J. Persistent Conjugated Backbone and Disordered Lamellar Packing Impart Polymers with Efficient n-Doping and High Conductivities. *Adv. Mater.* **2021**, *33*, 2005946.
(44) Karpov, Y.; Kiriy, N.; Formanek, P.; Hoffmann, C.; Beryozkina, T.; Hambsch, M.; Al-Hussein, M.; Mannsfeld, S. C. B.; Büchner, B.; Debnath, B.; Bretschneider, M.; Krupskaya, Y.; Lissel, F.; Kiriy, A. Sequentially Processed P3HT/CN6-CP●−NBu4+ Films: Interfacial or Bulk Doping? *Adv. Electron. Mater.* **2020**, *6*, 1901346.
(45) Arkhipov, V. I.; Emelianova, E. V.; Heremans, P.; Bässler, H. Analytic Model of Carrier Mobility in Doped Disordered Organic Semiconductors. *Phys. Rev. B* **2005**, *72*, 235202.
(46) Pingel, P.; Schwarzl, R.; Neher, D. Effect of Molecular P-Doping on Hole Density and Mobility in Poly(3-hexylthiophene). *Appl. Phys. Lett.* **2012**, *100*, 143303.
(47) Olthof, S.; Mehraeen, S.; Mohapatra, S. K.; Barlow, S.; Coropceanu, V.; Brédas, J.-L.; Marder, S. R.; Kahn, A. Ultralow Doping in Organic Semiconductors: Evidence of Trap Filling. *Phys. Rev. Lett.* **2012**, *109*, 176601.
(48) Shimotani, H.; Diguet, G.; Iwasa, Y. Direct Comparison of Field-Effect and Electrochemical Doping in Regioregular Poly(3-hexylthiophene). *Appl. Phys. Lett.* **2005**, *86*, 022104.
(49) Kronemeijer, A. J.; Pecunia, V.; Venkateshvaran, D.; Nikolka, M.; Sadhanala, A.; Moriarty, J.; Szumilo, M.; Sirringhaus, H. Two-Dimensional Carrier Distribution in Top-Gate Polymer Field-Effect Transistors: Correlation Between Width of Density of Localized States and Urbach Energy. *Adv. Mater.* **2014**, *26*, 728−733.
(50) Kim, S.; Ha, T.-J.; Sonar, P.; Dodabalapur, A. Density of Trap States in a Polymer Field-Effect Transistor. *Appl. Phys. Lett.* **2014**, *105*, 133302.
(51) Lang, D. V.; Chi, X.; Siegrist, T.; Sergent, A. M.; Ramirez, A. P. Amorphouslike Density of Gap States in Single-Crystal Pentacene. *Phys. Rev. Lett.* **2004**, *93*, 086802.
(52) Ho, C. H. Y.; Cheung, S. H.; Li, H.-W.; Chiu, K. L.; Cheng, Y.; Yin, H.; Chan, M. H.; So, F.; Tsang, S.-W.; So, S. K. Using Ultralow Dosages of Electron Acceptor to Reveal the Early Stage Donor-Acceptor Electronic Interactions in Bulk Heterojunction Blends. *Adv. Energy Mater.* **2017**, *7*, 1602360.
(53) Xiao, M.; Sadhanala, A.; Abdi-Jalebi, M.; Thomas, T. H.; Ren, X.; Zhang, T.; Chen, H.; Carey, R. L.; Wang, Q.; Senanayak, S. P.; Jellett, C.; Onwubiko, A.; Moser, M.; Liao, H.; Yue, W.; McCulloch, I.; Nikolka, M.; Sirringhaus, H. Linking Glass-Transition Behavior to Photophysical and Charge Transport Properties of High-Mobility Conjugated Polymers. *Adv. Funct. Mater.* **2020**, *31*, 2007359.
(54) Zhang, C.; Yuan, J.; Ho, J. K. W.; Song, J.; Zhong, H.; Xiao, Y.; Liu, W.; Lu, X.; Zou, Y.; So, S. K. Correlating the Molecular Structure of A-DA′D-A Type Non-Fullerene Acceptors to Its Heat Transfer and Charge Transport Properties in Organic Solar Cells. *Adv. Funct. Mater.* **2021**, *31*, 2101627.
(55) Wu, S.; Zhang, J.; Li, Z.; Liu, D.; Qin, M.; Cheung, S. H.; Lu, X.; Lei, D.; So, S. K.; Zhu, Z.; Jen, A. K.-Y. Modulation of Defects and Interfaces through Alkylammonium Interlayer for Efficient Inverted Perovskite Solar Cells. *Joule* **2020**, *4*, 1248−1262.
(56) Abraham, M. J.; Murtola, T.; Schulz, R.; Páll, S.; Smith, J. C.; Hess, B.; Lindahl, E. GROMACS: High Performance Molecular Simulations Through Multi-Level Parallelism from Laptops to Supercomputers. *SoftwareX* **2015**, *1*−*2*, 19−25.
(57) Noriega, R.; Rivnay, J.; Vandewal, K.; Koch, F. P. V.; Stingelin, N.; Smith, P.; Toney, M. F.; Salleo, A. A General Relationship Between Disorder, Aggregation and Charge Transport in Conjugated Polymers. *Nat. Mater.* **2013**, *12*, 1038−1044.
(58) Giri, G.; Verploegen, E.; Mannsfeld, S. C.; Atahan-Evrenk, S.; Kim, D. H.; Lee, S. Y.; Becerril, H. A.; Aspuru-Guzik, A.; Toney, M. F.; Bao, Z. Tuning Charge Transport in Solution-Sheared Organic Semiconductors Using Lattice Strain. *Nature* **2011**, *480*, 504−508.

Downloaded from pubs.acs.org/ancac3/article-pdf/20/15/11545/6504759/8/nn5c13008.pdf by PEKING UNIV user on 23 November 2026

https://doi.org/10.1021/acsnano.5c13008
ACS Nano 2026, 20, 11545−11557